A decarbonized vinyl chloride synthesis via selective oxidative coupling of methyl chloride

Yue Wang[1]†, Shihui Zou[1,2]*†, Abhinandan Nabera,[3]† Yang Pan[4], Xutao Chen[1], Kunkun Wei[1], Jingbo Hu[1], Yilin Zhao[1], Chengyuan Liu[4], Juanjuan Liu[5], Yong Wang[6], Gonzalo Guillén-Gosálbez,[3] Javier Pérez-Ramírez,[3]* Jie Fan[1]*

[1]Key Lab of Applied Chemistry of Zhejiang Province, Department of Chemistry, Zhejiang University, Hangzhou 310027, China.

[2]Department of Materials Science and Engineering, Zhejiang University of Technology, Hangzhou 310014, China.

[3]Institute for Chemical and Bioengineering, Department of Chemistry and Applied Biosciences, ETH Zürich, Vladimir-Prelog-Weg 1, Zurich 8093, Switzerland.

[4]National Synchrotron Radiation Laboratory, University of Science and Technology of China, Hefei 230029, China.

[5]College of Materials & Environmental Engineering, Hangzhou Dianzi University, Hangzhou 310036, China.

[6]Center of Electron Microscopy and State Key Laboratory of Silicon Materials, School of Materials Science and Engineering, Zhejiang University, Hangzhou 310027, China.

†These authors contributed equally to this work.

*Corresponding authors. E-mails: xueshan199@163.com (S.Z.); jpr@chem.ethz.ch (J.P.-R.); jfan@zju.edu.cn (J.F.)

Abstract: Selective coupling of C_1 platform molecules to C_2 olefins is a cornerstone for establishing a sustainable chemical industry based on non-petroleum sources. Vinyl chloride (C_2H_3Cl), one of top commodity petrochemicals, is commercially produced from coal- or oil-derived C_2 hydrocarbon (acetylene and ethylene) feedstocks with a high carbon footprint. Here, we report a decarbonized vinyl chloride synthesis via selective oxidative coupling of methyl chloride. This is enabled by a solid catalyst, featuring tungstate sub-nanoclusters embedded in a zirconia matrix, which effectively

captures ·CH_2Cl radicals homogeneously generated in CH_3Cl oxy-pyrolysis and selectively couples them into C_2H_3Cl. In-situ synchrotron-based vacuum ultraviolet photoionization mass spectrometry provides direct experimental evidence of the homogeneous-heterogeneous reaction mechanism. The process achieves methyl chloride conversion of 10 – 65% with a high vinyl chloride selectivity (60 – 75%) at a reaction temperature (600 – 750 °C), which is much lower than the traditional pyrolysis (> 850 °C). It also delivers a stable performance (at a vinyl chloride yield of *ca.* 30%) with no deactivation observed during a 50-hour test. Furthermore, combining with reaction of methanol and HCl to produce methyl chloride, we establish a methanol-to-vinyl chloride (MTV) route with the potential for significant reductions in climate change impact (24%) and cost (38%) compared to the state-of-the-art ethylene-based balanced process. A more remarkable 237% reduction in climate change impacts can be anticipated in the future-oriented green scenario for MTV process primarily attributed to the utilization of renewable C_1 feedstocks that results in negative net contributions to the overall impacts.

Main

Decarbonization is the next frontier of chemical industry. Vinyl chloride (C_2H_3Cl), the monomer of the third-most widely manufactured plastic, polyvinyl chloride, is produced commercially from fossil coal- or oil-derived C_2 hydrocarbon feedstocks[1-3]. The direct hydrochlorination of coal-derived acetylene leads to vinyl chloride monomer (VCM) using toxic $HgCl_2$ catalysts[4-6]. The ethylene-based balanced process (EBP) integrates the direct chlorination/oxychlorination of oil-derived ethylene and pyrolysis of ethylene dichloride (EDC) to produce VCM and has been widely adopted by VCM producers since the mid-1950s, accounting for nearly all capacities worldwide[7-9]. Although these industrial processes are suboptimal due to the use of relatively expensive and high carbon footprint feedstocks[9,10], a new reaction route that can rival the existing ones in terms of cost and environmental impact is still underdeveloped. Very recently, it has been demonstrated that using natural gas-derived ethane as the feedstock, VCM could be made at a cheaper cost and with less CO_2 emissions[9,11]. Yet,

an economically competitive decarbonized VCM production process based on the efficient utilization of cheaper and renewable C_1 feedstocks still represents a grand challenge.

C_1 platforms, such as methane, methanol, carbon monoxide, and carbon dioxide, play a crucial role in the current and future energy and chemical supply[12-14]. Their significance is expected to grow further due to the increasing need to decarbonize chemicals and fuels in line with CO_2 capture and utilization to mitigate global warming[13,15]. The coupling of C_1 molecules to C_2 olefins presents a sustainable alternative to the petroleum-based chemical industry. One such example is the conversion of methanol to hydrocarbons[16-20], which, when integrated with the renewable production of methanol from CO_2[21], sets the foundation for a methanol economy[22].

Herein, we report a methanol-based route for VCM production (MTV). The MTV process includes direct reaction of methanol and HCl to form methyl chloride (another important C_1 molecule[23-26]), followed by oxidative coupling of methyl chloride to make VCM (MCTV). The reactions for each component process are shown in **equation 1** and **2**, and the overall reaction is given by **equation 3**.

$$CH_3OH + HCl \rightarrow CH_3Cl + H_2O \quad (1)$$

$$2CH_3Cl + \frac{1}{2}O_2 \rightarrow C_2H_3Cl + HCl + H_2O \quad (2)$$

$$2CH_3OH + HCl + \frac{1}{2}O_2 \rightarrow C_2H_3Cl + 3H_2O \quad (3)$$

The hydrochlorination of methanol yields methyl chloride as the main product with small amounts of dimethyl ether as the only by-product. It is commercially carried out in both liquid-phase and gas-phase processes[27]. The second step (MCTV) is the key for MTV process and has not been established yet.

Results

CH_3Cl to C_2H_3Cl transformation

Direct coupling of CH_3Cl into VCM is theoretically feasible via radical chain reactions ($CH_3Cl \rightarrow {\cdot}CH_2Cl \rightarrow C_2H_4Cl_2 \rightarrow C_2H_3Cl$)[28]. However, there is no catalytic

way to steer CH_3Cl transformation at elevated temperature due to the highly reactive and short-lived nature of the radicals, the complex reaction networks, and uncontrollable gas-phase kinetics, especially in the presence of oxygen molecules (**Fig. 1**)[28]. Methyl chloride (oxy)pyrolysis is a high-temperature (> 850 °C) free radical chain process[29,30], in which $\cdot CH_2Cl$ and $\cdot CH_3$ are two key C_1 intermediates. Methyl chloride readily couples to form acetylene, ethylene and some VCM in the gas phase. However, the VCM yield in methyl chloride (oxy)pyrolysis is only 1 – 3% without replenishing chlorine in the pyrolysis system[31,32]. The loss of its chlorine component is due to facile VCM decomposition under the high-temperature condition[30,33]. Especially in the presence of oxygen, VCM is completely decomposed at temperature above 750 °C. In this work, we have discovered that high-concentration tungstate clusters embedded in a ZrO_2 matrix (NaWZr) can effectively capture $\cdot CH_2Cl$ homogeneously generated in CH_3Cl oxy-pyrolysis and selectively convert them into VCM. The proposed homogeneous-heterogeneous reaction mechanism is confirmed by in-situ synchrotron-based vacuum ultraviolet photoionization mass spectrometry (SVUV-PIMS). The oxidative coupling of methyl chloride into VCM achieves methyl chloride conversion of 10 – 60% with a high VCM selectivity (60 – 75%) at a reaction temperature (650 – 750 °C) much lower than traditional pyrolysis. The resulting VCM yield (8.9 – 39.7%) is massively propelled compared to that of the conventional pyrolysis (< 3%). Moreover, the utilization of renewable C_1 feedstocks (*e.g.*, green methanol and biomethane) leads to superior environmental and economic performance, demonstrating the potential for a *ca.* 25% reduction in climate change impacts and *ca.* 40% reduction in costs.

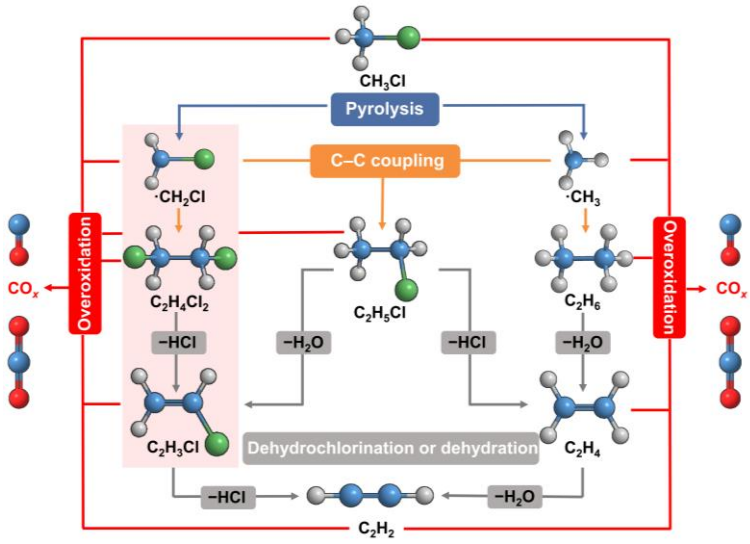

Fig. 1 | A brief overview of the reaction networks of CH_3Cl-to-C_2H_3Cl (MCTV) transformation.

The NaWZr catalyst was prepared by our recently developed co-precipitation method using WCl_6 and $Zr(OC_4H_9)_4$ as precursors and NaOH as precipitating agent[34]. A W-to-Zr molar ratio of 1:3 was adopted to achieve a high concentration of sodium tungstate clusters within the ZrO_2 matrix (see detailed methods in Supplementary Material). The final catalyst was calcined at 750 °C for 5 h before any characterization and catalytic tests. Aberration-corrected transmission electron microscopy confirms that W species are uniformly dispersed on the ZrO_2 matrix as sodium tungstate clusters and the average particle size of tungstate clusters is ~0.8 nm (**Fig. 2a** and **Supplementary Fig. 1**). For comparison, Na_2WO_4/ZrO_2 prepared by incipient-wetness impregnation shows a non-uniform distribution of W and Zr (**Supplementary Fig. 2**). Due to the high mass loading of impregnated Na_2WO_4 (~35%), only part of them can disperse as nanoclusters on the surface of ZrO_2 (**Supplementary Fig. 2**). The tungsten-rich/zirconium-poor regions in elemental mappings of Na_2WO_4/ZrO_2 evidence that the excess Na_2WO_4 aggregates into bulk crystals (**Supplementary Fig. 2**). Similar trends are also seen for NaWAl (**Supplementary Fig. 3**) and Na_2WO_4/Al_2O_3, demonstrating the co-precipitation

method as a superior method to impregnation for obtaining a higher concentration of sodium tungstate clusters.

The oxidative coupling of CH_3Cl was conducted at atmospheric pressure under an optimized condition (**Fig. 2c, Supplementary Fig. 4** and **5**) of CH_3Cl:O_2:N_2 = 1:2:57 and 650 – 750 °C that is much lower than traditional oxy-pyrolysis. There is no noticeable CH_3Cl conversion for the blank experiment at 750 °C, and the homogeneous reaction only attains limited CH_3Cl conversion (< 3.7%) and C_2H_3Cl selectivity (< 10%) even at 800 °C (**Fig. 2c** and **Supplementary Table 1**). Using ZrO_2 and Al_2O_3 as the catalysts significantly reduces the light-off temperature and improves CH_3Cl conversion but without C_2H_3Cl selectivity (< 1%) (**Fig. 2d** and **Supplementary Table 1**). Interestingly, once 35 wt.% of Na_2WO_4 is deposited onto ZrO_2 (Na_2WO_4/ZrO_2), a boosted ~18% C_2H_3Cl selectivity is obtained over a wide range of CH_3Cl conversion (blue shaded area in **Fig. 2e**). This result suggests Na_2WO_4 as the active component driving the pyrolysis of CH_3Cl to produce C_2H_3Cl. Moreover, when NaWZr and NaWAl with high concentrations of Na_2WO_4 clusters are used as the catalysts, the oxidative pyrolysis of CH_3Cl eventually involves into a selective coupling of CH_3Cl to C_2H_3Cl. As shown in the red shaded area in **Fig. 2e**, the C_2H_3Cl selectivity reaches 75.7% at CH_3Cl conversion of 10 – 20% (T = 650 °C) and maintains ~60% at CH_3Cl conversion of ~65% (T = 750 °C). Other minor products are CH_4 (0 – 3%), C_2H_4 (6 – 9%), C_2H_2 (0 – 7%), CO_2 (2 – 9%) and CO (8 –25%). A single-pass C_2H_3Cl yield as high as ~39.7% is achieved over NaWZr at 750 °C. Further increasing the reaction temperature results in a decrease of C_2H_3Cl yield to 23.3% due to facile VCM decomposition at higher reaction temperature. The NaWZr catalyst delivers stable CH_3Cl conversion and C_2H_3Cl selectivity during a 50-hour test (**Fig. 2f**). A stable 28% C_2H_3Cl yield is achieved at 700 °C. Aberration-corrected transmission electron microscopy analysis of the NaWZr catalyst after reaction confirms the structural stability of the sub-nanoclusters (**Supplementary Fig. 6**). Moreover, a C_2H_3Cl yield as high as 33% with a C_2H_3Cl selectivity of 53.9% can be achieved at 725 °C even without using N_2 as a dilution gas (**Supplementary Table 2**). The excellent C_2H_3Cl yield, low reaction temperature, and stable catalytic performance distinguishes MCTV with

traditional pyrolysis process and showcase the great potential of MCTV for industrial-scale C_2H_3Cl production.

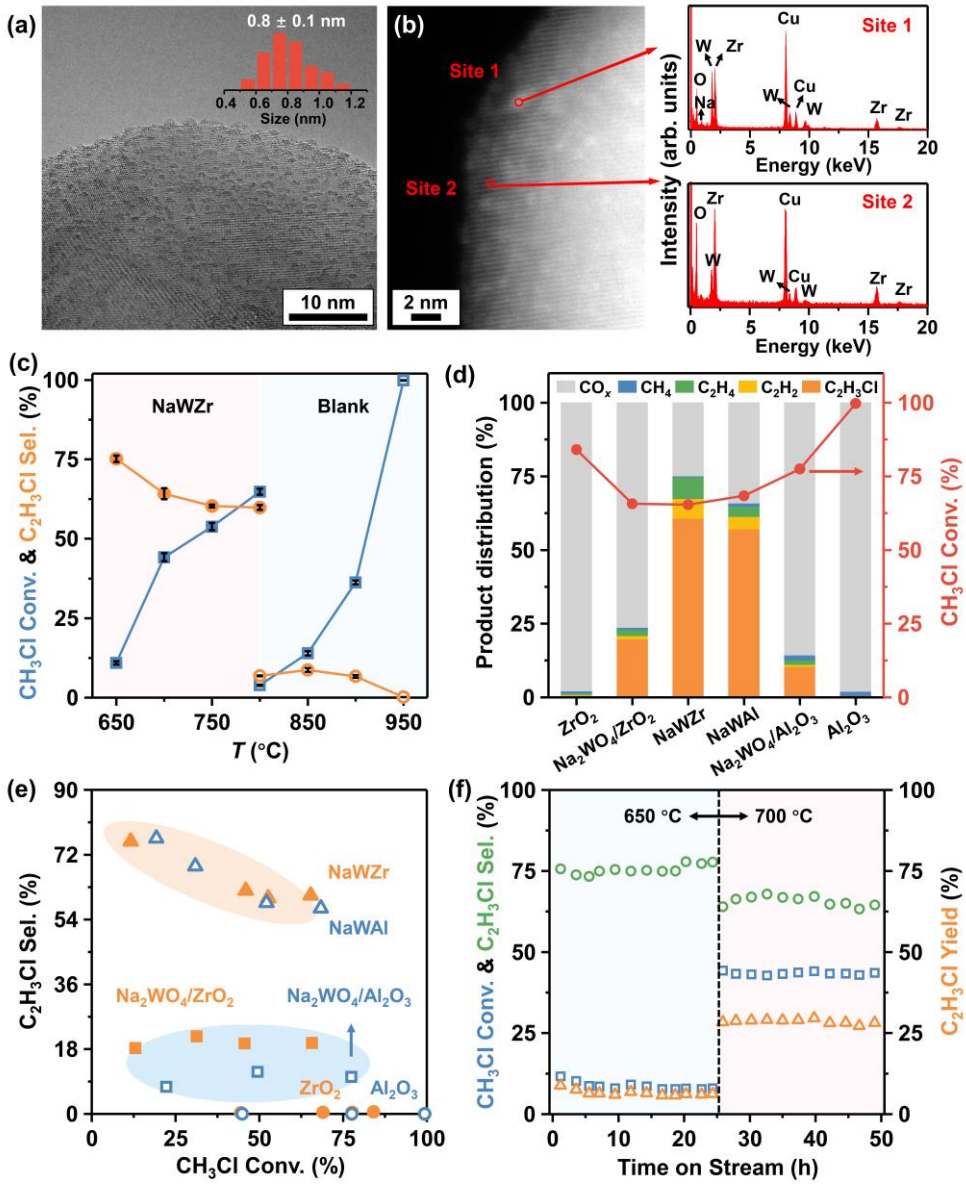

Fig. 2 | Structural characterization and reaction performance. (**a**) The aberration-corrected transmission electron microscopy images of NaWZr catalyst. (**b**) Representative energy dispersive spectroscopy (EDS) analysis of NaWZr catalyst. (**c**) CH_3Cl conversion and VCM selectivity as functions of reaction temperature in MCTV (NaWZr catalyst) and oxy-pyrolysis. The error bar was calculated based on three independent experiments. (**d**) The CH_3Cl conversion and product selectivity over various catalysts at 750 °C. (**e**) The catalytic performances of various catalysts in MCTV. Detailed data are summarized in **Supplementary Table 1**. (**f**) Long-term

stability tests over NaWZr catalyst at 650 and 700 °C. Reaction conditions: 150 mg catalyst, $CH_3Cl:O_2:N_2$ = 1:2:57, total gas flow rate = 60 mL min^{-1}.

We further investigate the compositional and structural influence of the tungstate catalyst in the CH_3Cl-to-C_2H_3Cl conversion. Replacing the W element in NaWZr by Mo decreases the C_2H_3Cl selectivity from ~60% to ~1%, demonstrating that tungsten is the core component of the active sites (**Supplementary Fig. 7**). Using ammonium metatungstate as the tungsten precursor in co-precipitation produces WO_3 instead of Na_2WO_4 (see X-ray diffraction patterns in **Supplementary Fig. 8**). The catalyst is denoted as WO_3-ZrO_2 and shows much lower C_2H_3Cl selectivity than NaWZr at all the temperatures evaluated (**Supplementary Fig. 9**), suggesting that the active sites for MCTV are Na_2WO_4 rather than WO_3. Notably, when the Na element in NaWZr is replaced by K, C_2H_3Cl selectivity decreases from ~60% to 22% (**Supplementary Fig. 7**), demonstrating the critical role of Na. It is interesting to note that bulk Na_2WO_4, whether physically mixed with ZrO_2 or not, exhibits a limited C_2H_3Cl yield (< 4%) over the investigated temperature range (**Supplementary Fig. 10**). Correlating this result with the high-angle annular dark field scanning transmission electron microscopy (HAADF-STEM) micrographs (**Supplementary Fig. 2)** and catalytic performance (**Fig. 2d**) of Na_2WO_4/ZrO_2 leads to the conclusion that Na_2WO_4 nanoclusters account for the C_2H_3Cl production. The higher concentration of Na_2WO_4 clusters in NaWZr than Na_2WO_4/ZrO_2 may therefore be responsible for the 3 – 4 times higher C_2H_3Cl selectivity at the same degree of CH_3Cl conversion **(Fig. 2e)**. To further verify this hypothesis, we synthesized a series NaWZr catalysts with different concentrations of Na_2WO_4 clusters and evaluated their catalytic performance in MCTV. According to our recent patent application[34], the Na_2WO_4 clusters concentration in NaWZr catalysts can be readily regulated by adjusting the W-to-Zr ratios and quantified by the number of tungstate clusters in 100 nm^2 of the ZrO_2 matrix in the high-resolution transmission electron microscopy (HRTEM) images. As shown in **Supplementary Fig. 11**, the volcano plots for the C_2H_3Cl selectivity and yield against the W-to-Zr ratio are similar to those for the concentration of tungstate nanoclusters. The maximum C_2H_3Cl selectivity and yield are achieved by NaWZr with W:Zr ratio of

3:9~4:9, which also shows the highest concentration of tungstate clusters. Notably, NaWAl using Al_2O_3 as support to anchor tungstate clusters also achieves high-concentration Na_2WO_4 clusters (**Supplementary Fig. 3**), and the catalytic performance of NaWAl is close to that of NaWZr (**Fig. 2** and **Supplementary Table 1**). These results exclude the support effect and hint at Na_2WO_4 nanoclusters as the active sites for MCTV.

Homogenous-heterogeneous mechanism

The oxidative pyrolysis of CH_3Cl to VCM proceeds via radical chain reactions at high temperatures (**Fig. 1**)[28]. Due to the lower bond strength of CH_3–Cl compared to CH_2Cl–H, chain radical initiation usually occurs via the endothermic decomposition of CH_3Cl into $\cdot CH_3$ and $\cdot Cl$ (**equation 4**).

$$CH_3Cl \rightarrow \cdot CH_3 + \cdot Cl, \Delta H = 83.3 \ \text{kcal mol}^{-1} \quad (4)$$

The subsequent exothermic H-abstraction reaction between $\cdot Cl$ and CH_3Cl (**equation 5**) dominates the conversion of CH_3Cl, yielding $\cdot CH_2Cl$ as the primary C_1 radical intermediate[29].

$$\cdot Cl + CH_3Cl \rightarrow \cdot CH_2Cl + HCl, \Delta H = -9.8 \ \text{kcal mol}^{-1} \quad (5)$$

$\cdot CH_2Cl$ can undergo coupling to form $C_2H_4Cl_2$ (**equation 6**), which readily decomposes into C_2H_3Cl and HCl (**equation 7**).

$$\cdot CH_2Cl + \cdot CH_2Cl \rightarrow C_2H_4Cl_2 \quad (6)$$

$$C_2H_4Cl_2 \rightarrow C_2H_3Cl + HCl \quad (7)$$

However, at elevated temperatures in the presence of oxygen, the irreversible overoxidation of reactive intermediates and products leads to a large amount of thermodynamically stable CO_x[29], which restricts the C_2H_3Cl selectivity and yield in oxidative pyrolysis (**Fig. 1**). Introducing NaWZr into the reaction system significantly changes the kinetics of oxidative pyrolysis, evidenced by the different apparent reaction orders of CH_3Cl (0.85 vs. 2.18, **Supplementary Fig. 12**) and reaction temperature. NaWZr achieves a CH_3Cl conversion of 46% at a significantly lower temperature than the blank experiment (700 °C versus 920 °C). More importantly, in the presence of

NaWZr, the reaction shifts from overoxidation to selective coupling into C_2H_3Cl at equivalent levels of CH_3Cl conversion (**Supplementary Fig. 13**).

To illustrate how NaWZr changes the kinetics of the oxidative pyrolysis of CH_3Cl, we investigated the impact of NaWZr on each elementary reaction of the CH_3Cl-to-C_2H_3Cl conversion. As shown in **Supplementary Fig. 14**, the decomposition of $C_2H_4Cl_2$ into C_2H_3Cl and HCl (**equation 7**) is a rapid reaction unaffected by the presence of NaWZr. Besides, the presence of CH_3Cl in gas phase significantly reduces the overoxidation of C_2H_3Cl, irrespective of the utilization of NaWZr as a catalyst (**Supplementary Fig. 15**). These findings exclude **equation 7** and the following conversion of C_2H_3Cl as the key steps influenced by NaWZr.

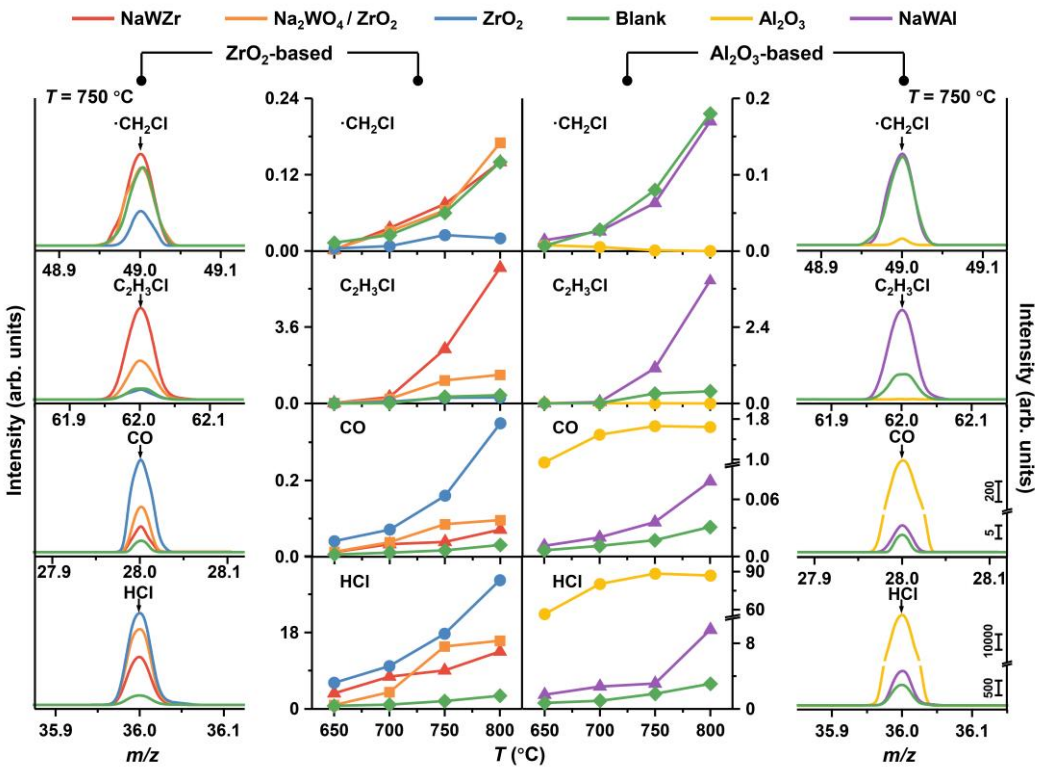

Fig. 3 | Evolution of representative species during reaction. The mass spectra of the representative species in the MCTV process were determined by in--situ SVUV-PIMS. Peak areas of the representative species were plotted as a function of temperature in the MCTV reaction over various catalysts. Reaction conditions: 150 mg catalyst, total pressure 0.1 bar, $CH_3Cl:O_2$ = 1:2, total gas flow rate = 60 mL min^{-1}.

The influence of NaWZr in radicals-involved elementary reactions was investigated by a validated in-situ synchrotron-based vacuum ultraviolet photoionization mass spectrometry (SVUV-PIMS)[35]. **Supplementary Fig. 16** displays all species detected at 750 °C and near ambient pressure (0.1 bar). Interestingly, the species identified during the blank experiment were also present over NaWZr, indicating their similar reaction pathways. Specifically, methyl (·CH_3) and chloromethyl radicals (·CH_2Cl), represented by the signals at *m/z* = 15 and 49, are observed, suggesting that in both cases the reaction proceeds via radical reactions. No $C_2H_4Cl_2$ and C_2H_5Cl signals were observed, likely due to their rapid decomposition into C_2H_3Cl and C_2H_4 (**Supplementary Fig. 14** and **17**). To elucidate the reaction mechanism, we quantitatively analyzed the evolution of key radical intermediates and representative products (·CH_2Cl, C_2H_3Cl, CO, and HCl) during the CH_3Cl-to-C_2H_3Cl conversion (**Fig. 3)**. The most important finding is that Na_2WO_4/ZrO_2, NaWZr, and NaWAl exhibit similar gas phase ·CH_2Cl signals but significantly higher C_2H_3Cl signals than the blank experiment over the investigated temperature range. According to the homogeneous reaction kinetics[35], the similar ·CH_2Cl concentration at the same reaction conditions would result in a similar reaction outcome in the gas phase. The distinct C_2H_3Cl signal would therefore result from the heterogeneous C_2H_3Cl production over tungstate catalysts. Moreover, the C_2H_3Cl signals follow the same trend of Na_2WO_4 clusters concentration, i.e., NaWZr > Na_2WO_4/ZrO_2 >> ZrO_2 ≈ blank. This result corresponds well with the catalytic data shown in **Fig. 2e** and **Supplementary Table 1** and further suggests that the heterogeneous C_2H_3Cl production occurs over Na_2WO_4 nanoclusters. The HCl signals at the same temperature follow an order of ZrO_2 > Na_2WO_4/ZrO_2 > NaWZr > blank, which is consistent with the trend of CH_3Cl conversion depicted in **Supplementary Table 1**. Given that Na_2WO_4 itself is inert for CH_3Cl activation over the investigated temperature range, the primary function of the catalyst in C_2H_3Cl production is the coupling ·CH_2Cl to form $C_2H_4Cl_2$ (**equation 6**), which readily decomposes into C_2H_3Cl and HCl.

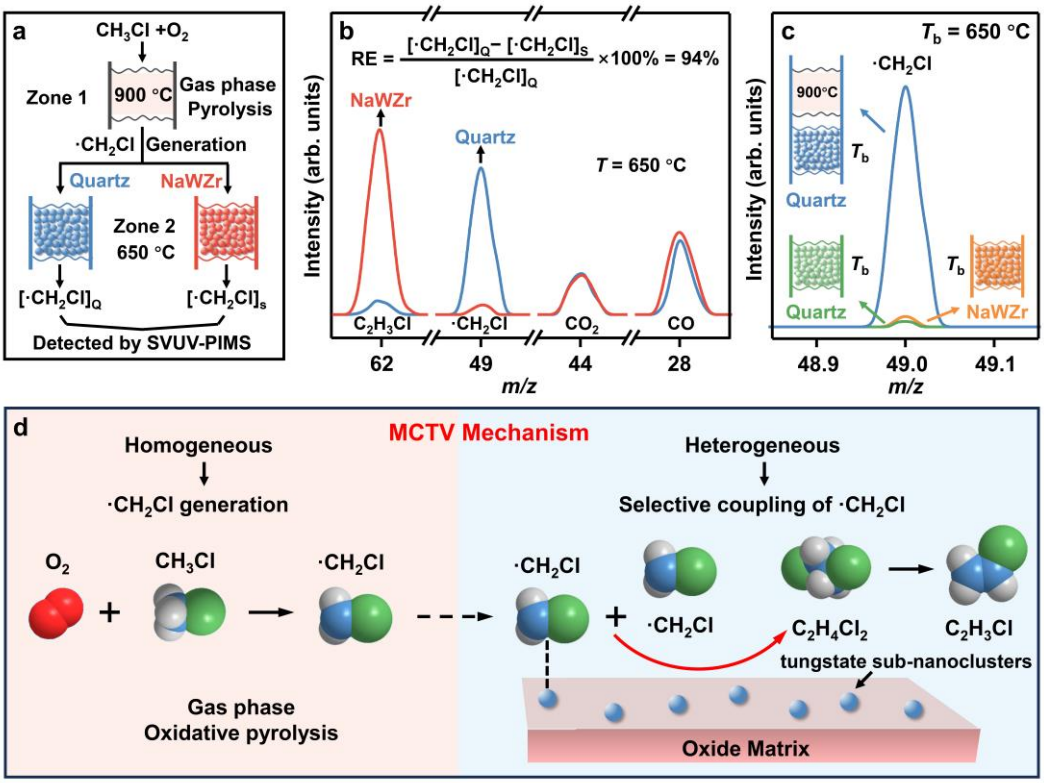

277

278 **Fig. 4 | Mechanistic analysis.** (**a, b**) The reaction efficiencies (RE) of NaWZr towards
279 ·CH_2Cl radicals generated by the oxidative pyrolysis of CH_3Cl in the gas phase at
280 900 °C. I_{NaWZr}/I_Q shows the intensity ratio of species detected over NaWZr and quartz.
281 (**c**) ·CH_2Cl detected by in-situ SVUV-PIMS over NaWZr and quartz at 650 °C.
282 Reaction conditions: 150 mg catalyst, P = 2.67 mbar, $CH_3Cl:O_2$ = 1:8, total gas flow
283 rate = 60 mL min^{-1}. (**d**) Schematic illustration of the homogeneous-heterogeneous
284 reaction mechanism of MCTV process.

285

286 To directly elucidate the homogeneous-heterogeneous mechanism of MCTV
287 reaction and investigate the critical role of NaWZr in controlling the transformation of
288 ·CH_2Cl, we designed a two-temperature-zone reactor for the in-situ SVUV-PIMS
289 study. In this reactor (**Fig. 4a)**, ·CH_2Cl was homogeneously generated by oxy-pyrolysis
290 of CH_3Cl at 900 °C (Zone 1) and then reacted with the downstream catalysts at 650 °C
291 (Zone 2). Quartz, an inert material for ·CH_2Cl generation and transformation
292 (**Supplementary Fig. 18**), was used as a control sample for NaWZr to offset the
293 homogeneous transformation of ·CH_2Cl in Zone 2. Gas-phase ·CH_2Cl and its products

after reacting with NaWZr and quartz were monitored by SVUV-PIMS in the low-pressure mode (2.67 mbar) to improve the signal-to-noise ratio. The minimal production of ·CH_2Cl (**Fig. 4c**) and HCl (**Supplementary Fig. 18**) from quartz and NaWZr at 650 °C (Zone 2) as compared to the oxidative pyrolysis of CH_3Cl at 900 °C (Zone 1) excluded their role in CH_3Cl activation to generate ·CH_2Cl and confirmed that the two-zone reactor configuration successfully separated ·CH_2Cl transformation from ·CH_2Cl generation. Interestingly, once ·CH_2Cl homogeneously generated by CH_3Cl (oxy)pyrolysis passed through NaWZr, its gas-phase concentration significantly declined (**Fig. 4b**). Following the definition of reaction efficiency (RE) proposed by Lunsford *et al*.[36], the RE of NaWZr towards ·CH_2Cl radicals was calculated to be 94%. These results unambiguously show that NaWZr can effectively capture ·CH_2Cl homogeneously generated by CH_3Cl oxy-pyrolysis and drive the following ·CH_2Cl transformation from the gas phase onto the catalyst surface. It is important to note that NaWZr produced 15 times higher C_2H_3Cl signal than quartz with only a slight increase of CO signal (6.7 %) (**Fig. 4b**). These results suggested that NaWZr is highly selective in capturing ·CH_2Cl and subsequently coupling them into $C_2H_4Cl_2$ (**equation 6**), which readily decompose into C_2H_3Cl and HCl. These critical surface elementary steps eventually change the reaction kinetics and prompt CH_3Cl conversion at low reaction temperature.

The surface-confined ·CH_2Cl transformation over Na_2WO_4 was also verified by the catalytic test over Na_2WO_4/SiO_2, which was prepared by incipient-wetness impregnation using quartz (SiO_2) as the support. As mentioned above, both quartz and Na_2WO_4 are inert for CH_3Cl activation. When Na_2WO_4/SiO_2 was used as the catalyst, ·CH_2Cl was generated solely from the homogeneous oxy-pyrolysis of CH_3Cl. Interestingly, Na_2WO_4/SiO_2 exhibited a remarkable CH_3Cl conversion and C_2H_3Cl selectivity at 700 °C (**Supplementary Fig. 19**). Meanwhile, all X-ray diffraction peaks of Na_2WO_4/SiO_2 can be well attributed to $Na_2WO_4{\cdot}2H_2O$ and SiO_2, excluding the phase transition of quartz and Na_2WO_4. These results confirmed that Na_2WO_4 are the active component in manipulating ·CH_2Cl transformation. The significantly higher CH_3Cl conversion as compared to the oxidative pyrolysis of CH_3Cl in the empty reactor (49.1%

versus ~0%), on the other hand, suggested that the effective capture and transformation of ·CH_2Cl over Na_2WO_4 can shift the chemical equilibrium of CH_3Cl oxy-pyrolysis towards ·CH_2Cl production. These findings further explained the significantly lower reaction temperature of NaWZr than the blank experiment for 46% CH_3Cl conversion (**Supplementary Fig. 13**).

In light of the aforementioned findings, the homogeneous-heterogeneous reaction mechanism of MCTV can be summarized as depicted in **Fig. 4d**. The reaction is initiated by a homogeneous ·CH_2Cl generation via oxy-pyrolysis, which is followed by a surface-confined ·CH_2Cl transformation to selectively produce C_2H_3Cl. This represents a significant advancement in controllable radical chemistry. Combined with commercial methyl chloride production via methanol and HCl reaction, we can establish an MTV process (methanol-to-VCM).

Environmental and economic assessment

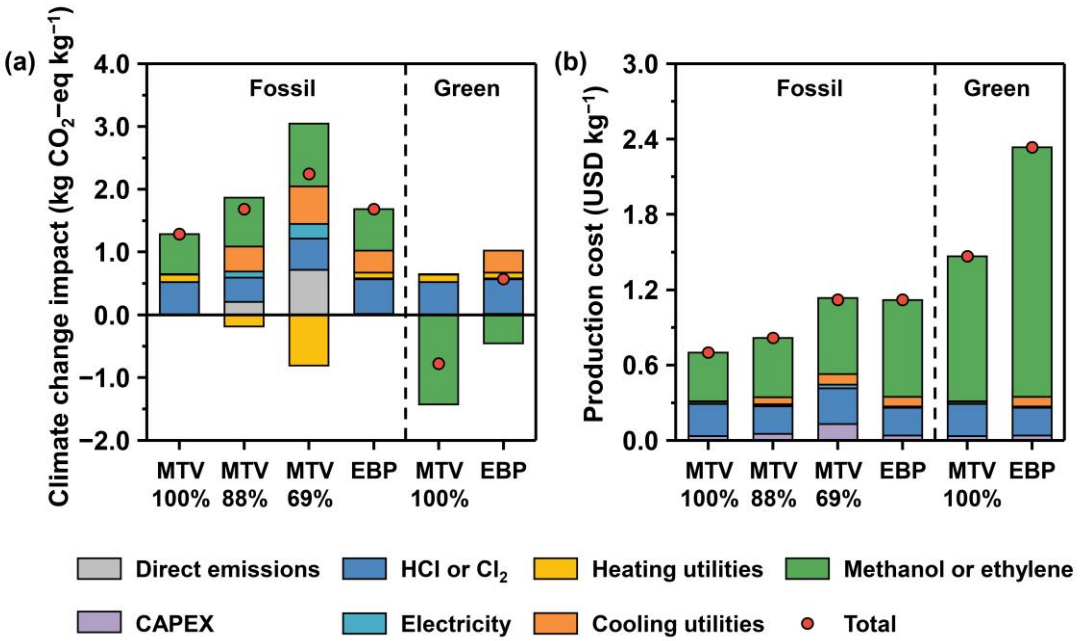

Fig. 5 | Environmental and economic comparison of processes for VCM manufacture. (a) Climate change impacts and **(b)** Production costs per kg of VCM *via* the MTV route (assuming different selectivities at current conversion, except for 100% where full conversion is considered) are compared to the conventional EBP pathway. The results for 88% and 69% selectivity are displayed as they correspond to the

scenarios for breakeven climate change impact and production cost in comparison to the EBP route, respectively. Results for both the fossil and green routes, depending on the hydrocarbon source, are shown. Bio-based hydrocarbon sources are discussed herein for the green routes, while other possible scenarios are displayed in **Supplementary Fig. 22**.

To further elucidate the practical significance of the MTV pathway on an industrial scale, we quantified its carbon footprint and production costs. Specifically, we compared the MTV process, assuming full conversion and selectivity to gauge its full potential (MTV 100%), with the conventional EBP route (ethylene-based balanced process for VCM synthesis). We considered two distinct scenarios for the MTV process, depending on the source of methanol: from natural gas reforming (fossil) and biomethane reforming (green). Similarly, for the EBP route, we explored two cases, distinguished by the source of ethylene: from steam reforming of hydrocarbons (fossil) and corn stover-based bioethanol dehydration (green). **Fig. 5a** displays the climate change impacts associated with the production of 1 kg of VCM. Notably, when comparing the fossil-based scenarios, we observed a substantial 24% reduction in carbon footprint. Furthermore, the switch to the green scenario, anticipated to be more applicable in the future, resulted in a significant 237% reduction in climate change impacts relative to the green ethylene analog. This substantial reduction in the future-oriented green scenario can be primarily attributed to the utilization of biomethane feedstock that results in negative net contributions to the overall impacts (on a cradle-to-gate basis) due to the biogenic nature of the carbon[37]. In addition to the reduction in the carbon footprint, both the current fossil-based and future green MTV scenarios demonstrated a 38% decrease in production costs relative to their ethylene-based counterparts (**Fig. 5b**). This reduction is predominantly due to the lower costs associated with C_1 feedstocks, specifically methanol (0.4 USD kg^{-1} for fossil methanol), compared to ethylene (1.7 USD kg^{-1} for fossil ethylene) used in the EBP route. Lastly, a sensitivity analysis on the MTV process revealed that the current selectivity is nearly at the target value of 69%, needed to match the economic

performance of the EBP pathway. Furthermore, with an 88% selectivity, the MTV route matches the climate change impacts of the EBP route, resulting in a 27% reduction in costs. Consequently, the MTV process represents a superior alternative in terms of both economic viability and environmental sustainability when compared to the state-of-the-art EBP route and will potentially play a pivotal role in establishing a more sustainable C_1 industry based on renewable carbon and less reliant on petroleum-derived sources.

Methods

Catalyst preparation

Synthesis of NaWZr. NaWZr was synthesized by a co-precipitation method using $Zr(OC_4H_9)_4$ and WCl_6 as the precursors[34]. Typically, 9 mmol of $Zr(OC_4H_9)_4$ and *X* mmol (*X* = 0 – 4) of WCl_6 were dissolved in 30 mL of ethanol to get a clear solution. Subsequently, a certain amount of NaOH aqueous solution (23 wt.%) was slowly added to the solution to generate precipitation. After stirring for 2 h, the mixture was transferred into a Petri dish (diameter 150 mm) to vapor the ethanol at 40 °C overnight. Afterward, the samples were aged at 85 °C for 6 h, followed by calcination at 750 °C for 5 h to get the final products. The W-to-Zr molar ratio of NaWZr is 3:9 if not elsewhere specified. NaWAl was synthesized by the same method with 9 mmol of $Al(OC_4H_9)_3$ mixed with 3 mmol of WCl_6 as the precursors. KWZr was synthesized by the same method with 9 mmol of $Zr(OC_4H_9)_4$ mixed with 3 mmol of WCl_6 as the precursors, then KOH aqueous solution (23 wt.%) was slowly added to the solution to generate precipitation. NaMoZr was synthesized by the same method with 9 mmol of $Zr(OC_4H_9)_4$ mixed with 3 mmol of $MoCl_5$ as the precursors.

Synthesis of WO_3-ZrO_2. WO_3-ZrO_2 was synthesized by the same co-precipitation method with 9 mmol of $Zr(OC_4H_9)_4$ mixed with 3 mmol of ammonium paratungstate.

Synthesis of Na_2WO_4/ZrO_2 catalyst. Na_2WO_4/ZrO_2 were prepared by an incipient-wetness impregnation method. 3 mmol of $Na_2WO_4{\cdot}2H_2O$ was dissolved in 10 mL of deionized water. Then 9 mmol of ZrO_2 was added into the clear solution. The mixture was stirred at 65 °C until dry, and then aged at 85 °C overnight. The acquired samples are denoted as Na_2WO_4/ZrO_2 after calcination at 750 °C for 5 h. Na_2WO_4/Al_2O_3 and Na_2WO_4/SiO_2 were synthesized by the same method.

Na_2WO_4, ZrO_2, Al_2O_3, and quartz sand (SiO_2) were purchased from the Aladdin Reagent Co. Ltd.

Catalyst characterization

High-angle annular dark field scanning transmission electron microscopy (HAADF-STEM) images and elemental mapping were acquired in an FEI Titan G2

80-200 ChemiSTEM microscope (200 kV) equipped with a spherical aberration corrector. High-resolution transmission electron microscopy (HRTEM) images were acquired in a spherical aberration (Cs)-corrected transmission electron microscope (FEI Titan G2 80-300) operating at an accelerating voltage of 300 kV. X-ray diffraction (XRD) patterns were recorded on a Rigaku Ultimate IV diffractometer using Cu Kα radiation at the 2θ angle range from 5 to 80°.

Synchrotron-based VUV photoionization mass spectrometry (SVUV-PIMS)

SVUV-PIMS study was carried out at the combustion beamline of the National Synchrotron Radiation Laboratory at Hefei, China. The quartz catalytic reactor was connected to the SVUV-PIMS system, where the catalyst bed was placed 60 mm away from the sampling nozzle (diameter 1.1 mm) of the mass spectrometer. All the catalysts (150 mg) were pelleted at 10 – 20 mesh before being loaded. CH_3Cl, O_2, and Ar in a ratio of 0.5:1:58.5 were cofed into the reactor with a total flow rate of 60 mL min^{-1}. The in-situ experiment was carried out at 0.1 bar. The signals of $\cdot CH_3$, $\cdot CH_2Cl$, C_2H_3Cl, and C_2H_4 were acquired at a photon energy of 10.7 eV, the signals of C_2H_2, $C_2H_2Cl_2$, CH_3Cl, and CH_2Cl_2 were acquired at a photon energy of 11.8 eV, the signals of H_2O, HCl, and CH_4 were acquired at a photon energy of 13 eV, and the signals of CO and CO_2 were collected with a photon energy of 14.6 – 14.8 eV.

Calculation of reaction efficiencies (RE) of NaWZr towards $\cdot CH_2Cl$ radicals

The secondary reactions of $\cdot CH_2Cl$ radicals over the catalysts could be quantified by reaction efficiencies (RE). CH_3Cl, O_2, and Ar in a ratio of 1.25:10:48.75 were cofed into a two-temperature-zone reactor with a total flow rate of 60 mL min^{-1}. $\cdot CH_2Cl$ radicals were generated by the oxidative pyrolysis of CH_3Cl in the gas phase at 900 °C (Zone 1), followed by reacting with 150 mg of down-stream catalysts (*e.g.*, NaWZr and quartz sand) at 650 °C (Zone 2). Gas-phase $\cdot CH_2Cl$ and its products after reacting with NaWZr and quartz were monitored by SVUV-PIMS in the low-pressure mode (2.67 mbar) to improve the signal-to-noise ratio.

RE is reported relative to quartz by using the equation:

$$\mathrm{RE} = \frac{[\cdot\mathrm{CH_2Cl}]_\mathrm{Q} - [\cdot\mathrm{CH_2Cl}]_\mathrm{S}}{[\cdot\mathrm{CH_2Cl}]_\mathrm{Q}} \times 100\% \quad (8)$$

Catalyst evaluation

Methyl chloride to vinyl chloride (MCTV): The MCTV tests were conducted in a quartz fix-bed reactor tube with a length of 300 mm and an inner diameter of 9 mm under atmospheric pressure. The tube was placed in the heating furnace vertically and configured with a thermocouple in the inner tube to detect the temperature. In a typical reaction, 150 mg of NaWZr catalyst was loaded in the reactor. CH_3Cl, O_2, and N_2 in a ratio of 1:2:57 were cofed into the reactor. The total flow rate was 60 mL min^{-1}. The products were analyzed by an online gas chromatography equipped with a flame ionization detector (FID) detector and a thermal conductivity detector (TCD) detector. CH_3Cl, CH_4, C_2H_4, C_2H_2, C_2H_3Cl were quantified by FID, and CO, CO_2 were quantified by TCD.

The contents of all the carbon-containing products were quantified by a standard curve method. The CH_3Cl conversion, products selectivity and yield were calculated using the following equations:

$$\mathrm{CH_3Cl\ \ Conv.} = \frac{X_{\mathrm{CH_3Cl,inlet}} - X_{\mathrm{CH_3Cl,outlet}}}{X_{\mathrm{CH_3Cl,inlet}}} \times 100\% \quad (9)$$

$$\mathrm{CH_4\ \ Sel.} = \frac{X_{\mathrm{CH_4,outlet}}}{X_{\mathrm{CH_3Cl,inlet}} - X_{\mathrm{CH_3Cl,outlet}}} \times 100\% \quad (10)$$

$$\mathrm{C_2H_4\ \ Sel.} = \frac{2 \times X_{\mathrm{C_2H_4,outlet}}}{X_{\mathrm{CH_3Cl,inlet}} - X_{\mathrm{CH_3Cl,outlet}}} \times 100\% \quad (11)$$

$$\mathrm{C_2H_2\ \ Sel.} = \frac{2 \times X_{\mathrm{C_2H_2,outlet}}}{X_{\mathrm{CH_3Cl,inlet}} - X_{\mathrm{CH_3Cl,outlet}}} \times 100\% \quad (12)$$

$$\mathrm{C_2H_3Cl\ \ Sel.} = \frac{2 \times X_{\mathrm{C_2H_3Cl,outlet}}}{X_{\mathrm{CH_3Cl,inlet}} - X_{\mathrm{CH_3Cl,outlet}}} \times 100\% \quad (13)$$

The C_2 products include C_2H_4, C_2H_2, and C_2H_3Cl.

$$\mathrm{C_2\ \ Sel.} = \frac{2 \times X_{\mathrm{C_2H_4,outlet}} + 2 \times X_{\mathrm{C_2H_2,outlet}} + 2 \times X_{\mathrm{C_2H_3Cl,outlet}}}{X_{\mathrm{CH_3Cl,inlet}} - X_{\mathrm{CH_3Cl,outlet}}} \times 100\% \quad (14)$$

$$\mathrm{CO\ \ Sel.} = \frac{X_{\mathrm{CO,intlet}}}{X_{\mathrm{CH_3Cl,inlet}} - X_{\mathrm{CH_3Cl,outlet}}} \times 100\% \quad (15)$$

$$\mathrm{CO_2\ \ Sel.} = \frac{X_{\mathrm{CO_2,outlet}}}{X_{\mathrm{CH_3Cl,inlet}} - X_{\mathrm{CH_3Cl,outlet}}} \times 100\% \quad (16)$$

$$\mathrm{C_2H_3Cl\ \ Yield} = \mathrm{CH_3Cl\ \ Conv.} \times \mathrm{C_2H_3Cl\ \ Sel.} \times 100\% \quad (17)$$

$$\mathrm{C_2\ \ Yield} = \mathrm{CH_3Cl\ \ Conv.} \times \mathrm{C_2\ \ Sel.} \times 100\% \quad (18)$$

The carbon balance was calculated according to:

$$\text{Carbon balance} = \frac{X_{CH_3Cl,outlet} + \sum x \times X_{products,outlet}}{X_{CH_3Cl,inlet}} \times 100\% \quad (19)$$

where x is the number of carbon atom in the products. (*i.e.*, CH_3Cl, CH_4, C_2H_4, C_2H_2, C_2H_3Cl, CO, CO_2). Generally, the carbon balance was higher than 98%.

$C_2H_4Cl_2$ oxidation: $C_2H_4Cl_2$ oxidation was conducted in the same reactor of MCTV. $C_2H_4Cl_2$ was pumped into the reactor at a flow rate of 0.5 mL h^{-1} and vaporized on the reactor wall prior to the catalytic bed. $C_2H_4Cl_2$, O_2, and N_2 in a ratio of 1:2:31 were cofed into the reactor. The total flow rate was 80 mL min^{-1}, and the mass of the catalyst was 150 mg. The C_2H_3Cl was quantified by a standard curve method. The C_2H_3Cl yield were calculated using the following equations:

$$C_2H_3Cl\ \text{Yield} = \frac{X_{C_2H_3Cl,outlet}}{X_{C_2H_2Cl_2,inlet}} \times 100\% \quad (20)$$

C_2H_5Cl oxidation: C_2H_5Cl oxidation were conducted in the same reactor of MCTV. C_2H_5Cl, O_2, and N_2 in a ratio of 1:2:57 were cofed into the reactor. The total flow rate was 60 mL min^{-1}. 150 mg of NaWZr catalyst was loaded in the reactor. The products were analyzed by an online gas chromatography equipped with an FID detector and a TCD detector. CH_4, C_2H_4, C_2H_2, CH_3Cl, C_2H_3Cl, C_2H_5Cl were quantified by FID, and CO, CO_2 were quantified by TCD. The contents of all the carbon-containing products were quantified by a standard curve method. The C_2H_5Cl conversion, products selectivity and yield were calculated using the following equations:

$$C_2H_5Cl\ \text{Conv.} = \frac{X_{C_2H_5Cl,inlet} - X_{C_2H_5Cl,outlet}}{X_{C_2H_5Cl,inlet}} \times 100\% \quad (21)$$

$$C_2H_4\ \text{Sel.} = \frac{X_{C_2H_4,outlet}}{X_{C_2H_5Cl,inlet} - X_{C_2H_5Cl,outlet}} \times 100\% \quad (22)$$

$$C_2H_3Cl\ \text{Sel.} = \frac{X_{C_2H_3Cl,outlet}}{X_{C_2H_5Cl,inlet} - X_{C_2H_5Cl,outlet}} \times 100\% \quad (23)$$

$$C_2H_4\ \text{Yield} = C_2H_5Cl\ \text{Conv.} \times C_2H_4\ \text{Sel.} \times 100\% \quad (24)$$

$$C_2H_3Cl\ \text{Yield} = C_2H_5Cl\ \text{Conv.} \times C_2H_3Cl\ \text{Sel.} \times 100\% \quad (25)$$

Economic and environmental assessment

The process models (**Supplementary Fig. 20** based on full conversion and

selectivity and **Supplementary Fig. 21** based on current conversion and selectivity) of the MTV route were developed in Aspen Plus v12, using standard unit operations to simulate reactions, temperature and pressure changes, and separations. The results of the simulation, including mass and energy inputs and outputs as well as sizes of process units, were then utilized for conducting an economic and environmental assessment. **Supplementary Table 3** and **4** display the mass balance of the MTV plant at full and current conversion and selectivity, respectively. The economic assessment considers operational and capital expenditures (OPEX and CAPEX) for the reference year 2022. The CAPEX and OPEX terms were calculated as in Medrano-García *et al*[38], from where we retrieved the economic performance of the EBP route. Specifically, the CAPEX term was determined using correlations from Sinnott and Towler[39], considering installation factors for each equipment unit and annualizing the total value using the annual capital charge ratio. **Supplementary Table 5** presents the prices of feedstock and utilities used in the OPEX estimation of both the MTV and EBP routes.

Next, the carbon footprint was quantified following an attributional life cycle assessment (LCA) in accordance with the ISO 14044/14040 standards[40,41]. The functional unit is 1 kg of VCM produced following a cradle-to-gate scope, including all activities from raw materials acquisition to the production of VCM at the plant. The cradle-to-gate scope is adopted because we assume that the end-use phase will be the same regardless of the synthesis route. The mass and energy flows of the EBP route were taken from Medrano-García *et al*.[38], while those for the MTV route were obtained from the process model developed in this work. These data enable us to model the foreground system (chemical plant), while data for modeling the background system (all activities supplying inputs to the chemical plant) were primarily sourced from the Ecoinvent v3.8 database[42]. We consider the 100-year global warming potentials (GWPs) as implemented in the IPCC 2013 methodology[43]. The inventories used to calculate the carbon footprint for both the MTV and EBP routes are shown in **Supplementary Table 6**. The breakeven selectivity of the fossil MTV route relative to the state-of-the-art EBP pathway (*i.e.*, the minimum selectivity considering the current conversion of 65.4% that would make the MTV process economically competitive

against the EBP analog) was obtained from a sensitivity analysis performed on the Aspen simulation based on current conversion and selectivity (*i.e.*, the current experimental values reported in this article).

Data availability

All the data supporting the findings of this study are available within the article and its Supplementary Information files or from the corresponding authors upon reasonable request.

References

1 Lin, R., Amrute, A. P. & Pérez-Ramírez, J. Halogen-mediated conversion of hydrocarbons to commodities. *Chem. Rev.* **117**, 4182-4247, (2017).

2 Kaiser, S. K. *et al.* Nanostructuring unlocks high performance of platinum single-atom catalysts for stable vinyl chloride production. *Nat. Catal.* **3**, 376-385, (2020).

3 Malta, G. *et al.* Identification of single-site gold catalysis in acetylene hydrochlorination. *Science* **355**, 1399-1403, (2017).

4 Hutchings, G. J. & Grady, D. T. Hydrochlorination of acetylene: The effect of mercuric chloride concentration on catalyst life. *Appl. Catal.* **17**, 155-160, (1985).

5 Johnston, P., Carthey, N. & Hutchings, G. J. Discovery, development, and commercialization of gold catalysts for acetylene hydrochlorination. *J. Am. Chem. Soc.* **137**, 14548-14557, (2015).

6 Schobert, H. Production of acetylene and acetylene-based chemicals from coal. *Chem. Rev.* **114**, 1743-1760, (2014).

7 Ma, H., Wang, Y., Qi, Y., Rout, K. R. & Chen, D. Critical review of catalysis for ethylene oxychlorination. *ACS Catal.* **10**, 9299-9319, (2020).

8 Ma, H. *et al.* Nitrogen-doped carbon-assisted one-pot tandem reaction for vinyl chloride production via ethylene oxychlorination. *Angew. Chem. Int. Ed.* **59**, 22080-22085, (2020).

9 Zichittella, G. & Pérez-Ramírez, J. Ethane-based catalytic process for vinyl chloride manufacture. *Angew. Chem. Int. Ed.* **60**, 24089-24095, (2021).

10 Ren, W. *et al.* Mercury transformation and distribution across a polyvinyl chloride (PVC) production line in China. *Environ. Sci. Technol.* **48**, 2321-2327, (2014).

11 Zichittella, G., Ceruti, A., Guillén-Gosálbez, G. & Pérez-Ramírez, J. Catalyst: A step forward for PVC manufacture from natural gas. *Chem* **8**, 883-885, (2022).

12 Amghizar, I., Vandewalle, L. A., Van Geem, K. M. & Marin, G. B. New trends in olefin production. *Engineering* **3**, 171-178, (2017).

13 Liu, Y., Deng, D. & Bao, X. Catalysis for selected C_1 chemistry. *Chem* **6**, 2497-2514, (2020).

14 Wei, Y., Zhang, D., Liu, Z. & Su, B.-L. Methyl halide to olefins and gasoline over zeolites and SAPO Catalysts: A new route of MTO and MTG. *Chin. J. Catal.* **33**, 11-21, (2012).

15 Mesters, C. A selection of recent advances in C1 chemistry. *Annu. Rev. Chem. Biomol. Eng.* **7**, 223-238, (2016).

16 Yang, M., Fan, D., Wei, Y., Tian, P. & Liu, Z. Recent progress in methanol-to-olefins (MTO) catalysts. *Adv. Mater.* **31**, e1902181, (2019).

17 Li, T., Shoinkhorova, T., Gascon, J. & Ruiz-Martínez, J. Aromatics production via methanol-mediated transformation routes. *ACS Catal.* **11**, 7780-7819, (2021).

18 Borodina, E. *et al.* Influence of the reaction temperature on the nature of the active and deactivating species during methanol-to-olefins conversion over H-SAPO-34. *ACS Catal.* **7**, 5268-5281, (2017).

19 Yarulina, I., Chowdhury, A. D., Meirer, F., Weckhuysen, B. M. & Gascon, J. Recent trends and fundamental insights in the methanol-to-hydrocarbons process. *Nat. Catal.* **1**, 398-411, (2018).

20 Olsbye, U. *et al.* Conversion of methanol to hydrocarbons: How zeolite cavity and pore size controls product selectivity. *Angew. Chem. Int. Ed.* **51**, 5810-5831, (2012).

21 Jiang, X., Nie, X., Guo, X., Song, C. & Chen, J. G. Recent advances in carbon dioxide hydrogenation to methanol via heterogeneous catalysis. *Chem. Rev.* **120**, 7984-8034, (2020).

22 Olah, G. A. Beyond oil and gas: The methanol economy. *Angew. Chem. Int. Ed.* **44**, 2636-2639, (2005).

587 23 Ibáñez, M. *et al.* Simultaneous coking and dealumination of zeolite H-ZSM-5
588 during the transformation of chloromethane into olefins. *Catal. Sci. Technol.* **6**, 296-
589 306, (2016).
590 24 Cesarini, A. *et al.* Elucidation of radical- and oxygenate-driven paths in zeolite-
591 catalysed conversion of methanol and methyl chloride to hydrocarbons. *Nat. Catal.* **5**,
592 605-614, (2022).
593 25 Terlingen, B. *et al.* Mechanistic insights into the lanthanide-catalyzed
594 oxychlorination of methane as revealed by operando spectroscopy. *ACS Catal.* **11**,
595 10574-10588, (2021).
596 26 Wei, Y., Zhang, D., Liu, Z. & Su, B.-L. Highly efficient catalytic conversion of
597 chloromethane to light olefins over HSAPO-34 as studied by catalytic testing and in
598 situ FTIR. *J. Catal.* **238**, 46-57, (2006).
599 27 Schmidt, S. A. *et al.* Methyl chloride synthesis over Al_2O_3 catalyst coated
600 microstructured reactor—Thermodynamics, kinetics and mass transfer. *Chem. Eng. Sci.*
601 **95**, 232-245, (2013).
602 28 Pelucchi, M. *et al.* Theoretical and kinetic modeling study of chloromethane
603 (CH_3Cl) pyrolysis and oxidation. *Int. J. Chem. Kinet.* **53**, 403-418, (2021).
604 29 Hung, S. L. & Pfefferle, L. D. A flow tube kinetics study of methyl chloride
605 oxidation. *Combust. Sci. Technol.* **87**, 91-107, (1993).
606 30 Granada, A., Karra, S. B. & Senkan, S. M. Conversion of methane into acetylene
607 and ethylene by the chlorine-catalyzed oxidative-pyrolysis (CCOP) process. 1.
608 Oxidative pyrolysis of chloromethane. *Ind. Eng. Chem. Res.* **26**, 1901-1905, (1987).
609 31 Marquaire, P.-M., Al Kazzaz, M., Muller, Y. & Just, J. S. Methane to vinyl chloride
610 by "Chloro-pyrolysis" of methyl chloride. *Stud. Surf. Sci. Catal.* **107**, 269-274, (1997).
611 32 Lombard, C. & Marquaire, P.-M. New study of methane to vinyl chloride process.
612 *Stud. Surf. Sci. Catal.* **147**, 529-534, (2004).
613 33 Weissman, M. & Benson, S. W. Pyrolysis of methyl chloride, a pathway in the
614 chlorine-catalyzed polymerization of methane. *Int. J. Chem. Kinet.* **16**, 307-333, (1984).
615 34 Fan, J., Wang, J., Zhou, Q. & Zou, S. Composite oxide containing tungstate
616 nanoclusters, and preparation method and application thereof. PCT/CN2021/124519

(2021).

35 Zou, S. *et al.* Surface coupling of methyl radicals for efficient low-temperature oxidative coupling of methane. *Chin. J. Catal.* **42**, 1117-1125, (2021).

36 Tong, Y., Rosynek, M. P. & Lunsford, J. H. Secondary reactions of methyl radicals with lanthanide oxides: Their role in the selective oxidation of methane. *J. Phys. Chem.* **93**, 2896-2898, (1989).

37 Rodin, V., Lindorfer, J., Böhm, H. & Vieira, L. Assessing the potential of carbon dioxide valorisation in Europe with focus on biogenic CO_2. *J. CO_2 Util.* **41**, 101219, (2020).

38 Medrano-García, J. D. *et al.* Economic and environmental competitiveness of ethane-based technologies for vinyl chloride synthesis. *ACS Sustain. Chem. Eng.* **11**, 13062-13069, (2023).

39 Towler, G. & Sinnott, R. *Chemical engineering design: principles, practice and economics of plant and process design*. (Butterworth-Heinemann, 2013).

40 International standards organization, Environmental management—Life cycle assessment—Principles and framework. ISO 14040:2006.

41 International standards organization, Environmental management—Life cycle assessment—Requirements and guidelines. ISO 14044:2006.

42 Wernet, G. *et al.* The ecoinvent database version 3 (part I): overview and methodology. *Int. J. Life Cycle Assess.* **21**, 1218-1230, (2016).

43 Field, C. B. & Barros, V. R. *Climate change 2014: Impacts, adaptation and vulnerability: Working Group II contribution to the fifth assessment report of the Intergovernmental Panel on Climate Change*. (Cambridge University Press, 2014).

Acknowledgements

This work was financially supported by National Natural Science Foundation of China grant (92045301, 91845203), National Key Research and Development Program of China grant (2022YFA1505500) and Shanxi-Zheda Institute of Advanced Materials and Chemical Engineering. The authors gratefully acknowledge Prof. Bo Yang and Jian Liu for helpful discussion.

Author contributions

†These authors contributed equally to this work. J.F. and S.Z. designed the study. Y.W., and S.Z. performed most of the experiments. Y.W., X.C., Y.Z., and J.L. synthesized the catalysts. Y.W., K.W., and Y.W. performed the structural characterization of catalysts. Y.W., Y.P., K.W., J.H., and C.L. performed the in-situ SVUV-PIMS study. A.N., G.G.-G. and J.P.-R. conceived, conducted, and analyzed the process simulations. Y.W., S.Z., A.N., G.G.-G., J.P.-R., and J.F. wrote the paper. The other authors performed some of the experiments and revised the paper.

Competing interests: JF, YW, SZ, FL and NL are named in patent applications (application numbers: CN202410208853.8) relating to this work. The remaining authors declare no competing interests.

Additional information

Supplementary Information accompanies this paper at https://doi.org/10.1038/xxxx.